

Understanding the rheology of kaolinite clay suspensions using Bayesian inference

Ranjiangshang Ran,¹ Shравan Pradeep,² Sébastien Kosgodagan Acharige,^{1,2} Brendan C. Blackwell,¹ Christoph Kammer,¹ Douglas J. Jerolmack,² and Paulo E. Arratia^{1,*}

¹*Department of Mechanical Engineering and Applied Mechanics,
University of Pennsylvania, Philadelphia, PA 19104, USA*

²*Department of Earth and Environmental Science,
University of Pennsylvania, Philadelphia, PA 19104, USA*

(Dated: October 25, 2022)

Abstract

Mud is a suspension of fine-grained particles (sand, silt, and clay) in water. The interaction of clay minerals in mud gives rise to complex rheological behaviors, such as yield stress, thixotropy and viscoelasticity. Here, we experimentally examine the flow behaviors of kaolinite clay suspensions, a model mud, using steady shear rheometry. The flow curves exhibit both yield stress and rheological hysteresis behaviors for various kaolinite volume fractions (ϕ_k). Further understanding of these behaviors requires fitting to existing constitutive models, which is challenging due to numerous fitting parameters. To this end, we employ a Bayesian inference method, Markov chain Monte Carlo (MCMC), to fit the experimental flow curves to a microstructural viscoelastic model. The method allows us to estimate the rheological properties of the clay suspensions, such as viscosity, yield stress, and relaxation time scales. The comparison of the inherent relaxation time scales suggests that kaolinite clay suspensions are strongly viscoelastic and weakly thixotropic at relatively low ϕ_k , while being almost inelastic and purely thixotropic at high ϕ_k . Overall, our results provide a framework for predictive model fitting to elucidate the rheological behaviors of natural materials and other structured fluids.

* Corresponding author: parratia@seas.upenn.edu

I. INTRODUCTION

Mud — a suspension of fine-grained particles (such as sand, silt, and clay) and water — forms the foundation of Earth’s surface and plays important roles in many natural (e.g., mudslides [1], soil erosion [2], river morphology [3, 4]) and industrial processes (e.g., civil construction [5], oil drilling [6]). At low stresses, mud exhibits solid-like behavior, which gives the material its load-bearing capacity. Above a certain threshold stress, however, these suspensions can experience sudden mechanical failure and start to flow like a liquid, as seen during the rapid and catastrophic mudslides [7]. This threshold at which the transition from solid- to fluid-like behaviors occurs is referred to as the “yield stress” [8–11]. Ultimately, to understand yielding behaviors in mud-like materials, we need models that can predict the yield stress of mud suspensions based on its constituents and bulk rheology. If successful, such rheological models could help improve failure predictions for industrial processes and prevent hazardous natural events.

The rheology of mud is dominated by the attractive nature of clay minerals, since these charged plate-shaped mud constituents are observed to aggregate and form gel-like microstructure [12–18]. This gives rise to “thixotropy” [19, 20], a rheological behavior characterized by time-dependent viscosity resulting from the evolution of the microstructure associated with flow history [21]. Thixotropic behaviors often involve two processes: an increase in viscosity due to the buildup of microstructure as the fluid is at rest (or “aging”), and a decrease in viscosity due to the breakdown of microstructure as the fluid is sheared (or “rejuvenation”) [22, 23]. Rheological models of thixotropy often use a structural parameter to relate the fluid microstructure to its macroscopic properties (e.g., viscosity), along with a kinetic equation to describe the evolution of the structural parameter [24–38]. A similar structural parameter and accompanied kinetic equation are also used to describe the rheological behaviors of “soft glassy” materials that are usually not referred to as thixotropic [39–46]. While the structural parameter is often taken to be a single scalar quantity [26–34, 37, 38], it can also be represented as tensors [25, 43, 46], scalar fields [44, 45], or a combination of multiple scalar quantities [35, 36]. Despite its clear physical meaning, the estimation of the structural parameter from experimental measurements is challenging.

Besides yield stress and thixotropy, mud and other clay-based suspensions can also exhibit viscoelasticity [47–50], since clay particles can form gel-like microstructure that behaves like weak elastic solids [21, 51, 52]. Viscoelastic behaviors are characterized by the relaxation of

elastic stress over an observed time scale [53]. The time scales associated with stress relaxation and microstructural evolution are usually different and independent, but it is often difficult to distinguish them [21–23, 37]. Therefore, to capture the rheological behaviors of mud and other structured fluids, such as food products [54–57] and crude oils [58, 59], constitutive models that incorporate both thixotropy and viscoelasticity are necessary [27–34, 36–46, 58, 59]. Such models commonly contain Maxwell- or Jeffrey-type viscoelastic elements whose viscosity and elasticity depend on the structural parameter. An exception is when the viscoelastic time scale (i.e., stress relaxation) is much shorter than that of thixotropic time scale (i.e., microstructural evolution), in which case the material is called “ideally” thixotropic and the effects of viscoelasticity can be neglected [22, 23, 35].

The interplay of thixotropy and viscoelasticity also leads to hysteresis behavior [45, 60–63]. A common procedure to identify such behavior is by sweeping the shear rate (or shear stress) downward and upward over a prescribed range [45, 60], which produces hysteresis loops in stress versus shear rate flow curves. This phenomenon is termed rheological hysteresis and has been widely reported in soft glassy materials such as clay, cement, and mud suspensions [60–69]. One way to quantify rheological hysteresis is by calculating the area enclosed by the hysteresis loops, i.e., hysteresis area [45, 60, 63, 65, 70, 71]. Since the rheological hysteresis depends on the magnitude and time step of the applied shear, the non-monotonic dependence of the hysteresis area as a function of time step can be used to infer the material’s intrinsic relaxation time scale [45, 60, 63, 70]. While such time scale has been associated with thixotropy, recent numerical simulations also observe the non-monotonic dependence of hysteresis area in purely viscoelastic materials [71]. Theoretically, the intrinsic time scales in materials that exhibit rheological hysteresis was studied using a fluidity model and the soft glassy rheology (SGR) model, which reproduce similar hysteresis behavior observed in the experimental systems [45, 61]. Alternatively, large amplitude oscillatory shear (LAOS) method is also reported in the literature to characterize the rheological hysteresis [32–34, 72–75]. Despite the advances in rheological models and measurements, it remains challenging to fit constitutive models to the experimental flow curves obtained from steady shear or LAOS, due to the model complexity and numerous fitting parameters. Therefore, common model fitting approaches often apply statistical methods such as Bayesian inference [76] and neural networks [77–80].

In this study, we experimentally examine the flow behaviors of kaolinite clay suspensions — a model mud — using shear rate sweep tests. The flow curves exhibit both yield stress

and hysteresis behaviors for different kaolinite volume fractions (ϕ_k). In an effort to understand these results, we fit the experimental flow curves to a constitutive model that is both viscoelastic and thixotropic, using Markov chain Monte Carlo (MCMC), a Bayesian inference method. The model fitting results provide estimates of the rheological properties of the clay suspensions, such as viscosity, yield stress, and inherent relaxation time scales. A comparison of the relaxation time scales of elastic stress and microstructure suggests that kaolinite clay suspensions are strongly viscoelastic and weakly thixotropic at relatively low ϕ_k , while they are almost ideally thixotropic and inelastic at high ϕ_k . Our results also reveal that kaolinite clay suspensions possess multiple time scales of stress and microstructural relaxation. Overall, our results provide insights into the development of the rheological models of natural materials such as mud and clay, as well as other structured fluids.

II. MATERIALS AND METHODS

A. Kaolinite clay suspensions

Kaolinite clay suspensions are prepared by dispersing natural kaolinite particles (03584 Sigma-Aldrich) into deionized water at four different volume fractions: $\phi = 0.05, 0.12, 0.19,$ and 0.26 . Kaolinite is a layered aluminum silicate ($\text{Al}_2\text{O}_3 \cdot 2\text{SiO}_2 \cdot 2\text{H}_2\text{O}$), which consists of stacks of individual plate-shaped particles (particle density, $\rho_p = 2.61 \text{ g/cm}^3$) joined together by hydrogen bonds. Kaolinite particles have a modal particle size, $d \approx 10 \text{ }\mu\text{m}$ [17, 81], and an aspect ratio $d/h \approx 10$, where h is the average thickness of the particles. The zeta potential of kaolinite particles at $\text{pH} = 7.0$ is estimated to be -30 mV [81], which indicates that kaolinite particles are weakly attractive and tend to aggregate in water.

B. Shear rate sweep test

A stress-controlled cone-plate rheometer (Bohlin, Malvern) is used to perform shear rate sweep tests that are similar to the protocols developed by Divoux *et al.* [60]. First, the sample is pre-sheared at a high shear rate ($\dot{\gamma}_{\text{max}}$) for 180 s to eliminate previous flow history and generate a reproducible initial microstructure. Next, two consecutive shear rate sweeps are performed: a downward sweep from the highest shear rate ($\dot{\gamma}_{\text{max}} = 10^3 \text{ s}^{-1}$) to the lowest shear rate ($\dot{\gamma}_{\text{min}} = 10^{-1} \text{ s}^{-1}$) through $N = 50$ logarithmically spaced steps of duration Δt each,

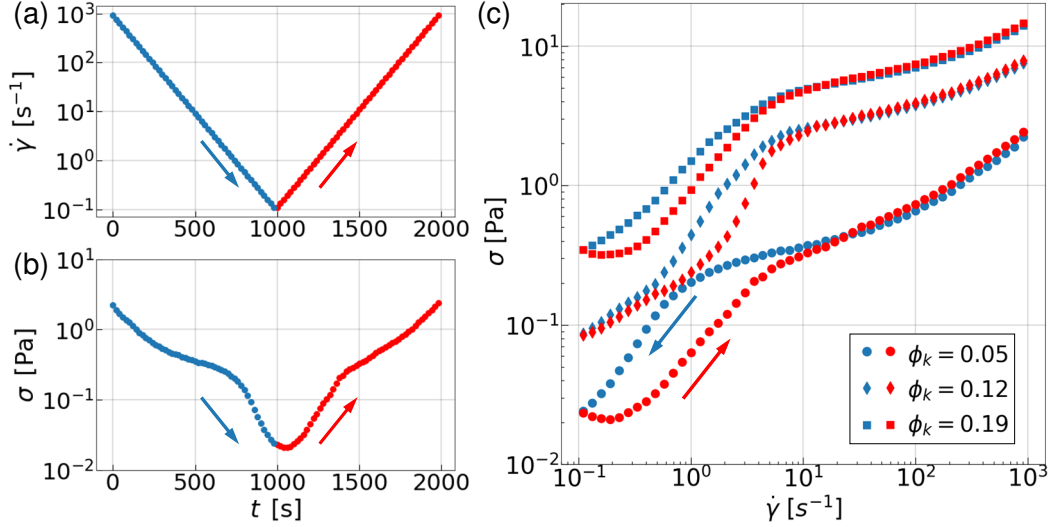


FIG. 1. (a) The prescribed shear rate ($\dot{\gamma}$) as a function of time in the shear rate sweep test: a downswEEP (blue) from $\dot{\gamma}_{\max} = 10^3 \text{ s}^{-1}$ to $\dot{\gamma}_{\min} = 10^{-1} \text{ s}^{-1}$ in 50 logarithmic steps of duration $\Delta t = 10 \text{ s}$ is followed by an upswEEP (red) from $\dot{\gamma}_{\min}$ back to $\dot{\gamma}_{\max}$ with the same steps in reverse order. (b) Experimental data for shear stress (σ) as a function of time t , for kaolinite suspension of $\phi_k = 0.05$ and $\Delta t = 10 \text{ s}$, showing an asymmetry in time. (c) Flow curves σ vs. $\dot{\gamma}$ for kaolinite suspensions of different volume fractions: $\phi_k = 0.05, 0.12, 0.19$, and $\Delta t = 10 \text{ s}$, showing rheological hysteresis behaviors.

followed by an upward sweep from $\dot{\gamma}_{\min}$ back to $\dot{\gamma}_{\max}$ with the same N logarithmic steps in a reverse order. In this manuscript, we adopt the terms “upswEEP” for the upward sweep in shear rates ($\dot{\gamma}_{\min} \rightarrow \dot{\gamma}_{\max}$) and “downswEEP” for the downward sweep in shear rates ($\dot{\gamma}_{\max} \rightarrow \dot{\gamma}_{\min}$), as used in previous literature [45]. Two different sweep time Δt are used: $\Delta t = 10 \text{ s}$ and 20 s , leading to total experimental duration of $2N\Delta t = 2000 \text{ s}$ and 4000 s , respectively. Figure 1(a) shows the prescribed shear rate as a function of time for $\Delta t = 10 \text{ s}$. The room temperature is maintained at $21 \text{ }^\circ\text{C}$ during all the tests.

Figure 1(b) shows the measured stress in a shear rate sweep test, for kaolinite suspension of volume fraction $\phi = 0.05$ and $\Delta t = 10 \text{ s}$. We find that the suspension stress is asymmetric in time even though the applied shear rate is symmetric in time 1(a); this asymmetry leads to rheological hysteresis in the σ - $\dot{\gamma}$ flow curves. Figure 1(c) shows examples of the rheological hysteresis behaviors for kaolinite suspensions of different volume fractions: $\phi = 0.05, 0.12$, and 0.19 with $\Delta t = 10 \text{ s}$. At low $\dot{\gamma}$, the suspension stress in upswEEP (red) lies below the downswEEP (blue) but beyond a critical shear rate ($\dot{\gamma}_c$) the flow curves reverse their behavior.

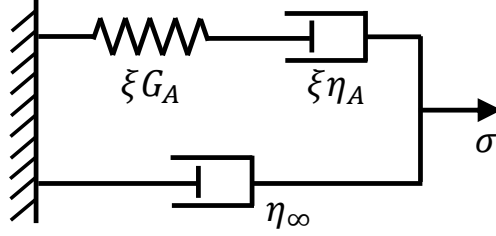


FIG. 2. A mechanical analog of the canonical three-element viscoelastic thixotropic model.

C. Rheological model

A viscoelastic thixotropic model [32] is used here to capture the clay suspensions' rheological behavior described above. The model is represented by a simple three-element Jeffreys canonical form in Fig. 2, where a constant infinite shear viscosity (η_∞) is modeled in parallel with a viscoelastic Maxwell component that is dependent on a scalar structural parameter, ξ . The viscous and elastic parts of the Maxwell component are assumed to be linearly dependent on the structural parameter as $\xi\eta_A$ and ξG_A , respectively, where η_A is the structural viscosity and G_A is the elastic modulus. The time evolution of the shear stress σ under an applied shear rate $\dot{\gamma}$ in a Jeffreys-type fluid can be described as:

$$\sigma + \lambda \frac{d\sigma}{dt} = (\eta_\infty + \xi\eta_A) \left(\dot{\gamma} + \lambda_r \frac{d\dot{\gamma}}{dt} \right), \quad (1)$$

where the fluid has a total viscosity $\eta = \eta_\infty + \xi\eta_A$, a single relaxation time $\lambda = \eta_A/G_A$ independent of microstructure, and a microstructural-dependent retardation time $\lambda_r = \lambda\eta_\infty/(\eta_\infty + \xi\eta_A)$. Equation (1) can be further reduced to the following form [32, 33]:

$$\frac{\sigma}{\eta_A} + \frac{1}{G_A} \frac{d\sigma}{dt} = \left(\xi + \frac{\eta_0}{\eta_A} \right) \dot{\gamma} + \frac{\eta_\infty}{G_A} \frac{d\dot{\gamma}}{dt}. \quad (2)$$

We assume homogeneous flow conditions in our model, and thus Equations (1) and (2) are given in the scalar form.

The time-evolution of the suspension microstructure is described using a kinetic equation of the form [24]:

$$\frac{d\xi}{dt} = k_A(1 - \xi) - k_R |\dot{\gamma}| \xi, \quad (3)$$

where ξ is a dimensionless structural parameter that ranges between 0 and 1 representing the unstructured and fully structured states, respectively. Equation (3) describes two different processes associated with the evolution of microstructure, namely “aging” and “rejuvenation”, represented by the kinetic rate constants, k_A and k_R , respectively. Aging is a spontaneous

buildup of microstructure when the fluid is undisturbed; and rejuvenation refers to a flow-induced breakdown of microstructure when the fluid is under shear [21]. To minimize the number of fitting parameters, we use the combination of Equations (2) and (3) to provide a minimal model of viscoelastic thixotropy. In this model, there is a total of 5 fitting parameters: infinite-shear viscosity (η_∞), structural viscosity (η_A), elastic modulus (G_A), aging rate constant (k_A), and rejuvenation rate constant (k_R). Despite the simplicity of this model, we still need a statistical inference method to fit it to the experimental flow curves, as discussed in Sec. IID.

D. Markov chain Monte Carlo (MCMC) method

Due to the relatively large number of fitting parameters, we need a statistical inference method to fit the proposed rheological model to our experimental data. To this end, we use the Markov chain Monte Carlo (MCMC) method, which is a class of algorithms that can generate a sequence of random samples from a probability distribution where direct sampling is difficult. To setup the problem, we consider a model \mathcal{M} determined by a set of parameters $\vec{\theta}$ that can make predictions on data $\vec{\mathcal{D}}$. Here, \mathcal{M} is the five-parameter rheological model proposed in the previous section with parameters $\vec{\theta} = [\eta_\infty, \eta_A, G_A, k_A, k_R]$, and the data $\vec{\mathcal{D}} = \{\sigma, \dot{\gamma}\}$; where the latter contains the experimentally measured shear stress and shear rate. The parameters $\vec{\theta}$ have a probability density $\mathbb{P}(\vec{\theta})$ satisfying some prior distributions, or initial guess. The distribution of interest is the posterior distribution of the density $\mathbb{P}(\vec{\theta}|\vec{\mathcal{D}})$, or the probability that the parameters $\vec{\theta}$ can provide the best model \mathcal{M} given the data $\vec{\mathcal{D}}$. We can compute this probability from Bayes' theorem:

$$\mathbb{P}(\vec{\theta}|\vec{\mathcal{D}}) = \frac{\mathbb{P}(\vec{\mathcal{D}}|\vec{\theta})\mathbb{P}(\vec{\theta})}{\mathbb{P}(\vec{\mathcal{D}})}, \quad (4)$$

where $\mathbb{P}(\vec{\mathcal{D}}) = \int \mathbb{P}(\vec{\mathcal{D}}|\vec{\theta})\mathbb{P}(\vec{\theta}) d\vec{\theta}$ is a normalizing constant [82]. The parameters that can best fit the experimental data are the ones maximizing Equation (4), which is given as:

$$\vec{\theta}_{\text{best}} = \underset{\vec{\theta}}{\operatorname{argmax}} \left\{ \mathbb{P}(\vec{\mathcal{D}}|\vec{\theta})\mathbb{P}(\vec{\theta}) \right\}, \quad (5)$$

and also known as the maximum likelihood estimation (MLE).

For the five-parameter model used here, an explicit formula of the posterior probability $\mathbb{P}(\vec{\theta}|\vec{\mathcal{D}})$ is difficult to obtain, and direct sampling from $\mathbb{P}(\vec{\theta}|\vec{\mathcal{D}})$ is computationally prohibitive. Hence, we resort to stochastic sampling methods (MCMC) to generate observations from the posterior distribution [76]. Specifically, we use the Metropolis-Hastings (M-H) algorithm that

was developed by Metropolis *et al.* [83] and later generalized by Hastings [84]. A standard procedure of the M-H algorithm to generate a Markov chain consisting of the following steps:

Step 0. Propose an initial guess $\vec{\theta} = \vec{\theta}_0$.

Step 1. Denote the current state as $\vec{\theta}$; propose a new state $\vec{\theta}'$ according to a transition kernel $q(\vec{\theta} \rightarrow \vec{\theta}')$.

Step 2. Calculate the acceptance ratio transitioning from $\vec{\theta}$ to $\vec{\theta}'$:

$$\alpha = \min \left(1, \frac{\mathbb{P}(\vec{\mathcal{D}}|\vec{\theta}')\mathbb{P}(\vec{\theta}')}{\mathbb{P}(\vec{\mathcal{D}}|\vec{\theta})\mathbb{P}(\vec{\theta})} \right). \quad (6)$$

Step 3. Draw an arbitrary number u from a uniform distribution $\mathcal{U}[0, 1]$. If $u < \alpha$, accept the new state $\vec{\theta} = \vec{\theta}'$; otherwise reject $\vec{\theta}'$ and keep $\vec{\theta} = \vec{\theta}$. Return to Step 1.

Here, the transition kernel $q(\vec{\theta} \rightarrow \vec{\theta}')$ is chosen to be a random walk:

$$q(\vec{\theta} \rightarrow \vec{\theta}') : \vec{\theta}' = \vec{\theta} + \mathcal{A}\vec{\epsilon}, \quad (7)$$

where $\vec{\epsilon} \sim \mathcal{N}(0, \epsilon_{\text{rw}}^2 \mathbf{I})$ is a normally distributed dimensionless perturbation vector, with ϵ_{rw} being a measure of step size of the random walk and \mathbf{I} being the identity matrix; \mathcal{A} is a diagonal matrix adapting the step size in different dimensions [85, 86], since all five parameters of $\vec{\theta}$ have different orders of magnitude and units.

The prior distribution of $\vec{\theta}$ is assumed to be normal: $\vec{\theta} \sim \mathcal{N}(\vec{\theta}_0, \epsilon_\theta^2 \mathcal{A})$, where ϵ_θ is a measure of uncertainty in the prior distribution, and \mathcal{A} is diagonal so that the components of $\vec{\theta}$ are independent. The posterior distribution of $\vec{\theta}$ relies on the definition of $\mathbb{P}(\vec{\mathcal{D}}|\vec{\theta})$. We denote the experimental data as $\vec{\mathcal{D}}$, and the data generated by model \mathcal{M} with parameters $\vec{\theta}$ as $\vec{\mathcal{D}}'$. We can then calculate the “distance” between $\vec{\mathcal{D}}$ and $\vec{\mathcal{D}}'$ by a metric ρ , defined as:

$$\rho(\vec{\mathcal{D}}, \vec{\mathcal{D}}') = \|\log(\sigma) - \log(\sigma')\|, \quad (8)$$

where $\|\cdot\|$ denotes the L^2 -norm, and σ and σ' are the experimental and model predicted shear stresses, respectively. Here, we use the logarithmic stress $\log(\sigma)$ to put an equal weight to the stress data of low shear rates, which is order of magnitude smaller than that of high shear rates. Note that the structural parameter ξ is not included in Equation (8) despite being predicted by the model \mathcal{M} , because ξ is unobservable in the experiments. Alternative methods quantifying the prediction of unobserved quantities can be found in [87]. Ideally, the metric $\rho(\vec{\mathcal{D}}, \vec{\mathcal{D}}')$ is

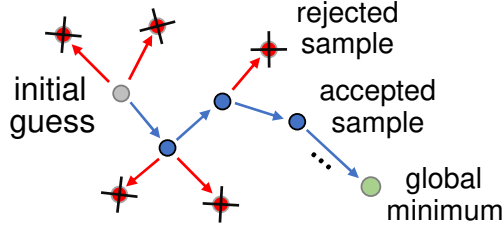


FIG. 3. A graphical representation of the MCMC method, M-H algorithm.

zero for a “perfect” model. We assume the metric is normally distributed with a zero mean: $\rho(\vec{\mathcal{D}}, \vec{\mathcal{D}}') \sim \mathcal{N}(0, \epsilon_\rho^2)$, therefore we have the conditional probability:

$$\mathbb{P}(\vec{\mathcal{D}}|\vec{\theta}) = \left(1/\sqrt{2\pi}\epsilon_\rho\right) \exp\left(-\rho^2(\vec{\mathcal{D}}, \vec{\mathcal{D}}')/2\epsilon_\rho^2\right). \quad (9)$$

To visualize the aforementioned MCMC method in a simple manner, a graphical representation of M-H algorithm is shown in Fig. 3. Starting with the initial guess $\vec{\theta}_0$ (gray dot), the current sample $\vec{\theta}$ performs a random walk to a new location $\vec{\theta}'$. Samples with low α are rejected (red dots marked with X), while samples with high α are accepted and recorded (blue dots). The Markov chain composed of all accepted samples will slowly drift towards the MLE that maximizes the posterior probability $\mathbb{P}(\vec{\theta}|\vec{\mathcal{D}})$, or global minimum in terms of the loss function of the predicted variables (green dot). The Markov chain will then fluctuate around the MLE and reach a stationary distribution. One can use the recorded samples from a stationary Markov chain to approximate the posterior distribution $\mathbb{P}(\vec{\theta}|\vec{\mathcal{D}})$. Figure 4(a) shows an example of a stationary Markov chain in a three-dimensional subspace of η_∞ , η_A , and G_A , for the model fitting of a kaolinite suspension at $\phi = 0.05$. The recorded samples (blue dots) are used to generate marginal probability densities (colormap). Figure 4(b) shows the evolution of parameters η_∞ , η_A , and G_A as a function of the number of iterations for the same kaolinite suspension at $\phi = 0.05$, starting with an initial guess of an order of magnitude estimation given as $\vec{\theta}_0 = [\eta_\infty, \eta_0, G_A] = [10^{-3} \text{ Pa.s}, 10^{-1} \text{ Pa.s}, 10^{-3} \text{ Pa}]$, the Markov chain becomes stationary in approximately 2000 iterations. Samples taken before the Markov chain is stationary are discarded. Only the samples in stationary Markov chain are used for the model prediction shown here.

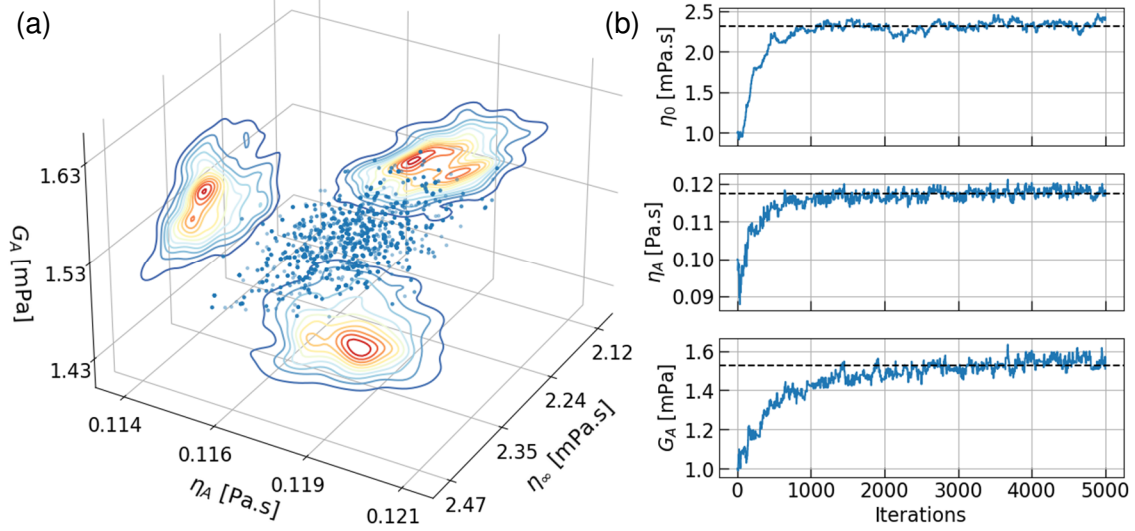


FIG. 4. (a) Accepted samples (blue dots) from a Markov chain for the fitting of a kaolinite suspension of $\phi = 0.05$, in a three-dimensional subspace of η_∞ , η_A , and G_A of the five-dimensional parametric space. Projections (colormap) are marginal density functions. (b) Evolution of the parameters η_∞ , η_A , and G_A for a kaolinite suspension of $\phi = 0.05$ as a function of iteration number. The Markov chain becomes stationary after around 2000 iterations.

III. RESULTS AND DISCUSSIONS

A. Model parameter fitting results

We first discuss the fitting results of the five model parameters that provide estimates of the rheological properties of kaolinite clay suspensions. Table I summarizes the values of the five model parameters: η_∞ , η_A , G_A , k_A , k_R (see Sec. II C), for different kaolinite volume fractions ϕ_k and sweep time Δt . Also listed are the critical shear rate $\dot{\gamma}_c$ and yield stress σ_y values which are discussed in Sec. III B. Since MCMC method provides the probability distributions of model parameters, we report both the mean and the standard deviation in Table I. Figures 5(a) and 5(b) show the uncertainty bounds for the model fittings of the stress (σ) and the structural parameter (ξ), respectively.

For all the ϕ_k values, the fitting parameter, the infinite-shear viscosity (η_∞) for kaolinite clay suspensions, is much larger than the viscosity of water ($\eta_w = 10^{-3}$ Pa.s). For example, the kaolinite suspension of the lowest volume fraction ($\phi = 0.05$) has a infinite-shear viscosity of $\eta_\infty \approx 2\eta_w$. The structural viscosity (η_A) of the clay suspensions is approximately 50 to 200 times the η_∞ . Both η_∞ and η_A increase nonlinearly with ϕ_k . As the sweep time increases from

TABLE I. Fitting results of the five model parameters: η_∞ , η_A , G_A , k_A , k_R ; also listed are critical shear rate $\dot{\gamma}_c$ and yield stress σ_y . All results are reported with 3 significant figures.

ϕ_k	$\eta_\infty \times 10^3$ [Pa.s]	η_A [Pa.s]	$G_A \times 10^3$ [Pa]	$k_A \times 10^3$ [s ⁻¹]	$k_R \times 10^3$ [-]	$\dot{\gamma}_c = k_A/k_R$ [s ⁻¹]	σ_y [Pa]
$\Delta t = 10$ s							
0.05	2.33 ± 0.05	0.114 ± 0.002	1.53 ± 0.08	17.1 ± 1.1	4.03 ± 0.28	4.31 ± 0.09	0.481 ± 0.007
0.12	4.26 ± 0.32	0.451 ± 0.006	11.6 ± 0.7	18.7 ± 5.6	2.14 ± 0.19	8.74 ± 0.24	3.90 ± 0.08
0.19	11.4 ± 0.4	1.82 ± 0.02	36.8 ± 0.9	11.2 ± 0.9	3.30 ± 0.25	3.36 ± 0.05	6.07 ± 0.05
0.26	131 ± 11	2.48 ± 0.02	1650 ± 260	11.7 ± 0.8	0.629 ± 0.041	18.6 ± 1.8	43.7 ± 0.3
$\Delta t = 20$ s							
0.05	2.27 ± 0.06	0.091 ± 0.001	0.84 ± 0.02	17.0 ± 0.8	2.80 ± 0.14	6.07 ± 0.12	0.538 ± 0.008
0.12	3.78 ± 0.29	0.405 ± 0.004	6.72 ± 0.13	8.02 ± 0.63	0.751 ± 0.082	10.7 ± 0.3	4.31 ± 0.08
0.19	9.11 ± 0.07	1.63 ± 0.02	19.6 ± 0.8	7.19 ± 0.31	1.83 ± 0.07	3.93 ± 0.04	6.39 ± 0.02
0.26	122 ± 10	2.26 ± 0.03	1260 ± 360	6.42 ± 0.42	0.310 ± 0.022	20.7 ± 2.5	44.2 ± 0.5

$\Delta t = 10$ s to 20 s, we find that the values of both the viscosities η_∞ and η_A decrease slightly by $\sim 5\%$ for all ϕ_k values. This is the result of the suspension exhibiting thixotropy [21–23], where the viscosity decreases as the suspension is sheared for a longer time.

Next, we find that the kinetic rate constants k_R and k_A are (on average) reduced by half (except for $\phi = 0.05$ for k_R) for all kaolinite clay suspensions as Δt increases from 10 s to 20 s. Nonetheless, the ratio between these two rate constants, $\dot{\gamma}_c = k_A/k_R$, increases by approximately 15%. The physical meaning of the ratio $\dot{\gamma}_c$ is discussed in Sec. III B. The changes in k_R and k_A with different Δt reveal that: (i) kaolinite clay suspensions have multiple time scales corresponding to the relaxation of microstructure; and (ii) the model captures only the dominant time scales corresponding to aging (k_A^{-1}) and rejuvenation ($|k_R \dot{\gamma}|^{-1}$). As Δt increase from 10 s to 20 s, the dominant time scales increase and the values of k_A and k_R decrease. Moreover, we find that the values of elastic moduli (G_A) are halved, on average, as Δt is doubled. This indicates that kaolinite clay suspensions have more than a single stress relaxation time scale, $\lambda = \eta_A/G_A$; and the value of λ for $\Delta t = 20$ s is almost twice as long as that for $\Delta t = 10$ s since η_A remains roughly a constant as Δt increases (see Table II). The multi-timescale nature of kaolinite clay suspensions, as well as the changes in these time scales with ϕ_k are discussed

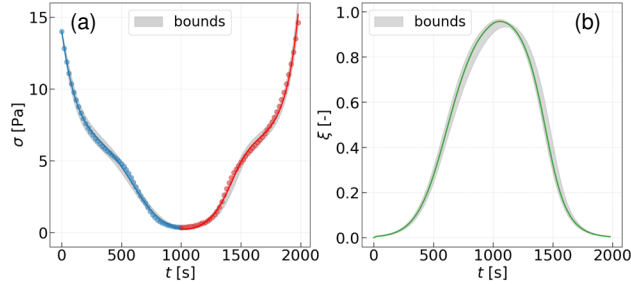


FIG. 5. Experimental data (dots) and model fittings (solid curves) of (a) stress (σ) and (b) structural parameter (ξ) as a function of time for a kaolinite suspension at $\phi = 0.19$. Gray shades are uncertainty bounds of the fitting results.

in more detail in Sec. III C.

B. Yield stress and rheological hysteresis behaviors

In this section, we focus on the yield stress and rheological hysteresis behaviors exhibited in the stress (σ) *vs.* shear rate ($\dot{\gamma}$) flow curves, and how well our model captures these behaviors. Figures 6(a) and 6(b) show the experimental data and model fitting results of σ - $\dot{\gamma}$ flow curves in linear-linear scale, for kaolinite suspensions of $\phi = 0.05$ and 0.19, respectively. We find that the stress increases rapidly with the shear rate until it reaches a critical stress value σ_y ; above σ_y , the stress exhibits a power-law-like relation with the shear rate. These are typical behaviors of a yield stress fluid, which are captured by the model fitting. Unlike equations of the Herschel-Bulkley form [88]: $\sigma = \sigma_0 + K\dot{\gamma}^n$, our model does not include an explicit yield stress σ_0 in the equation of stress [Equation (2)]. Rather, the model captures the yield stress behaviors through a dramatic decrease in viscosity from $(\eta_A + \eta_\infty)$ to η_∞ with increasing shear rate. Nevertheless, one can estimate a yield stress from the model as: $\sigma_y = (\eta_A - \eta_\infty)\dot{\gamma}_c$, where $\dot{\gamma}_c = k_A/k_R$ is a critical shear rate at which the material starts to fluidize [32]. We can see that the model predicted yield stress σ_y is located relatively accurately at the yield transition of the flow curves for both ϕ_k [red dashed lines in Fig. 6(a) and 6(b)]. Above yield, the stress during upsweep (red) overshoots and stays higher than the stress during downsweep (blue). This rheological hysteresis behavior is also captured by the model. Table I lists the values of the yield stress σ_y for different volume fraction ϕ_k and sweep time Δt . We find that σ_y increases nonlinearly with the volume fraction ϕ_k , since the additional kaolinite particles increase the viscosities η_A and η_∞ . As Δt is doubled, σ_y stays roughly the same (Table I), which suggests the yield stress of

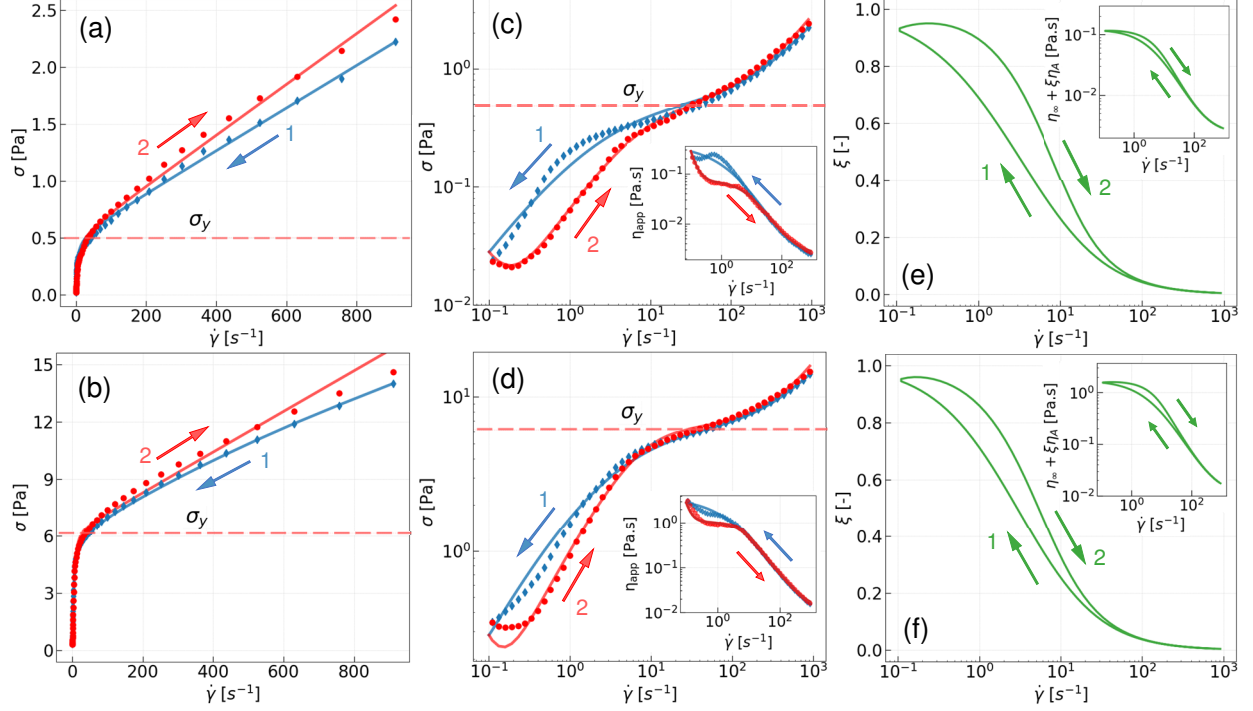


FIG. 6. (a-b) Stress σ vs. shear rate $\dot{\gamma}$ flow curves in linear-linear scale, for kaolinite suspensions of different volume fractions: (a) $\phi = 0.05$ and (b) $\phi = 0.19$. Arrows indicate the direction of the shear rate sweep: first a downsweep (blue, “1”), followed by an upsweep (red, “2”). Symbols are experimental data; solid curves are fittings of the rheological model. Yield stress σ_y is indicated by red dashed lines. (c-d) The same flow curves as in (a) and (b), but in log-log scale, for (c) $\phi = 0.05$ and (d) $\phi = 0.19$. Insets: apparent viscosity, $\eta_{\text{app}} = \sigma/\dot{\gamma}$, of the same flow curves. (e-f) structural parameter ξ as a function of $\dot{\gamma}$, obtained from the model fittings, for (e) $\phi = 0.05$ and (f) $\phi = 0.19$. Insets: actual viscosity of the same data, $\eta = \eta_\infty + \xi\eta_A$.

kaolinite clay suspensions is approximately time-independent.

Figures 6(c) and 6(d) highlights the rheological behaviors of kaolinite suspensions below yield stress, by showing the same flow curves as in Fig. 6(a) and 6(b) but in log-log scale. At low shear rate, we find that the stress during upsweep (red) undershoots and stays below that during downsweep (blue), until it reaches the yield stress. This creates a hysteresis loop below yield that is inverted compared to the flow curves above yield, in which case the stress overshoots during upsweep. Our model captures this double-loop hysteresis behaviors quite well. Similar double-loop hysteresis behaviors have been observed for other structured fluids in previous studies [45, 57]. And it has been proposed that the looping behavior below yield

is the signature of viscoelasticity [45]: the elastic stress initially accumulated at the high shear rates continues to relax during upsweep, which leads to lower stress values during upsweep than downsweep. This mechanism requires the time scale of stress relaxation to be comparable to the time scale of microstructural relaxation; and we shall see that this is the case for kaolinite suspensions at these volume fractions in Sec. III C. Overall, these results suggest that the behaviors of kaolinite clay suspensions are primarily viscoelastic below yield transition, which is consistent with previous modelling of structured fluids [28, 29].

Insets of Figs. 6(c) and 6(d) show the apparent viscosity, $\eta_{\text{app}} = \sigma/\dot{\gamma}$, of the same flow curves. We find that η_{app} increases non-monotonically during downsweep (blue), which is likely due to the coexistence of multiple stress relaxation times. This non-monotonic behavior is not captured by our model, since our model only has a single stress relaxation time λ . During upsweep (red), the model fits the flow curves relatively better than downsweep. This can be understood as follows. Since elastic stress is mainly accumulated at the start of downsweep, faster stress relaxation modes have already fully relaxed at the end of downsweep. And our model captures the longest relaxation time λ associated with the slowest stress relaxation mode during upsweep. Another limitation of the model is that it only has a single microstructural relaxation time k_A^{-1} , thus it fails to predict non-monotonic microstructural relaxation behaviors [38]. Both limitations of our model can be responsible for the discrepancy between the experimental data and the model fittings. These results suggest that structural kinetic models with multiple relaxation time scales may better capture the rheological behavior of clay suspensions, especially the non-monotonic relaxation behaviors in Fig. 6(c) and 6(d). It has been shown that viscoelastic models with multiple stress relaxation times can capture non-monotonic stress relaxation behaviors, examples including the soft glassy rheology (SGR) model [39, 40, 45] and the mode coupling theory (MCT) model [53, 89]. It has also been shown that model with multiple microstructural relaxation time scales are able to capture non-monotonic thixotropic relaxation behaviors, such as the multimode structural kinetics model [35, 36].

Figures 6(e) and 6(f) show the structural parameter ξ as a function of shear rate $\dot{\gamma}$, for kaolinite suspensions of $\phi_k = 0.05$ and 0.19. Since ξ is unobservable, there is no experimental data shown in the figures. We find that for all shear rates, the structural parameter during upsweep (“2”) is always larger than that during downsweep (“1”), leading to hysteresis loops in the ξ - $\dot{\gamma}$ flow curves. Since the fluid viscosity is directly related to the structural parameter by $\eta = \eta_\infty + \xi\eta_A$, the viscosity during the upsweep is also always higher than that during

downsweep, as shown in the insets of Fig. 6(e) and 6(f). This is expected since downsweep has a much stronger shear history than upsweep: the high $\dot{\gamma}$ values at the start of downsweep destroy most microstructure in the fluid, while the low $\dot{\gamma}$ values at the beginning of upsweep allow more microstructure to build up. These results provide further evidence that the hysteresis behaviors in Figs. 6(c) and 6(d) are caused by viscoelasticity. The fluid has a lower stress value despite having a higher viscosity during upsweep (than downsweep), which indicates the looping behaviors below yield stress are the results of viscoelasticity, instead of the change in viscosity due to thixotropy.

C. Stress *vs.* microstructural relaxation time scales

Kaolinite suspensions exhibit thixotropy since kaolinite clay particles form microstructure in the suspensions that physically breaks down and builds up over time [16–18, 90]. In our model, there are two time scales associated with thixotropy: k_A^{-1} for the buildup (or relaxation) of microstructure, and $|k_R \dot{\gamma}|^{-1}$ for the breakdown of microstructure. Despite the former is often termed “thixotropic time scale” in the literature [23, 64, 70], here we refer to k_A^{-1} as the “microstructural relaxation time scale” to distinguish between the two different time scales associated with thixotropy. In this section, we focus on the comparison of two relaxation time scales: λ associated with the relaxation of elastic stress, and k_A^{-1} associated with the relaxation of microstructure in the suspension. The ratio between the two time scales, λk_A , provides a possible classification of thixotropy into “ideal” and “viscoelastic” [21–23]. “Ideal” thixotropic materials have a much shorter relaxation time of elastic stress than that of microstructure, and $\lambda k_A \rightarrow 0$; “viscoelastic” thixotropic materials have a stress relaxation time that is comparable to the microstructural relaxation time, and $\lambda k_A \sim \mathcal{O}(10^0)$.

Table II lists the fitting results of the stress relaxation time λ , the microstructural relaxation time k_A^{-1} , and the ratio between the two time scales λk_A , for different volume fractions ϕ_k and sweep time Δt . We first discuss the changes in these time scales with ϕ_k . We find that both time scales are at the order of 30 seconds to several minutes (except for $\phi_k = 0.26$, which is discussed later). The stress relaxation time λ decreases with increasing ϕ_k , while the microstructural relaxation time k_A^{-1} increases with ϕ_k . As a result, the time scale ratio λk_A decreases with ϕ_k , indicating that the kaolinite suspensions become more thixotropic and less viscoelastic. An exception is for $\Delta t = 20$ s, at $\phi_k = 0.12$ and $\phi_k = 0.19$. We believe that this is due to the multi-

TABLE II. Stress relaxation time scale λ , microstructural relaxation time scale k_A^{-1} , and the ratio between the 2 time scales λk_A .

ϕ_k	λ [s]	k_A^{-1} [s]	λk_A [-]
$\Delta t = 10$ s			
0.05	77.0 ± 5.4	58.7 ± 3.7	1.32 ± 0.07
0.12	38.8 ± 1.4	54.0 ± 5.6	0.73 ± 0.06
0.19	49.5 ± 3.4	93.1 ± 4.5	0.56 ± 0.02
0.26	1.5 ± 0.4	85.4 ± 6.4	0.02 ± 0.00
$\Delta t = 20$ s			
0.05	107.3 ± 1.7	59.1 ± 2.8	1.82 ± 0.08
0.12	60.8 ± 2.7	125.8 ± 6.5	0.49 ± 0.05
0.19	83.1 ± 3.7	139.4 ± 5.8	0.60 ± 0.01
0.26	1.8 ± 0.6	156.2 ± 7.2	0.01 ± 0.00

timescale nature of kaolinite clay suspension, which will be explained later in the discussion of Fig. 7. At relatively low volume fractions ($\phi_k < 0.26$), $\lambda k_A \sim \mathcal{O}(10^0)$. At the highest volume fraction ($\phi_k = 0.26$), however, λk_A decreases dramatically to $\sim \mathcal{O}(10^{-2})$, which indicates the kaolinite suspension is almost ideally thixotropic with negligible viscoelasticity. The changes in the rheological behaviors of kaolinite suspensions can be explained as follows. Kaolinite particles are charged platelets; the faces and edges of kaolinite particles carry opposite charges. As ϕ_k increases, the dominant interaction between kaolinite particles transitions from an edge-face attraction to a face-face repulsion, due to steric effects [17]. This transition from attractive to repulsive interaction will reduce the viscoelastic behaviors of kaolinite suspensions [91], which is responsible for the dramatic decreases in λ (from ~ 30 s to ~ 1 s) and λk_A (from ~ 0.5 to ~ 0.01) at the highest ϕ_k .

Next, we focus on the changes in stress and microstructural relaxation times with different sweep time Δt . We find that both time scales λ and k_A^{-1} increase as Δt is doubled from 10 s to 20 s (by an average of 53% and 68%, respectively). As discussed in Sec. III A, this is a result of the multi-timescale nature of kaolinite clay suspensions, as they possess multiple stress and microstructural relaxation times. Since the model used here only has a single stress relaxation time λ and a single microstructural relaxation time k_A^{-1} , it captures only the dominant time

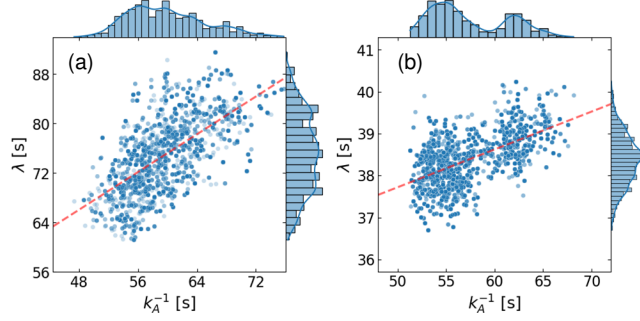


FIG. 7. (a) Examples of kaolinite suspensions possessing linearly correlated spectra of stress relaxation time scale λ and microstructural relaxation time scale k_A^{-1} , for $\phi_k = 0.05$ and $\Delta t = 10$ s. (b) Examples of kaolinite suspensions possessing a single dominant stress relaxation time scale λ , and multiple dominant microstructural relaxation time scales k_A^{-1} , for $\phi_k = 0.12$ and $\Delta t = 10$ s. Here, joint distributions are illustrated by scatter plots of the accepted samples from the Markov chain (blue dots), and marginal distributions are shown by the histograms on the side (bar plots); red dashed lines are linear regressions of the data.

scales of the relaxation processes. As Δt increases, the dominant time scales captured by the model will increase accordingly, which is shown by the increase in stress and microstructural relaxation times with Δt (Table II). Since λ and k_A^{-1} increase by roughly the same percentage, the ratio between them λk_A^{-1} remains similar as Δt is increased.

Another piece of evidence of the multi-timescale nature of kaolinite suspensions can be shown by the probability distribution phase of the relaxation time scales. Figure 7(a) shows the joint probability distribution of λ and k_A^{-1} for $\phi = 0.05$ and $\Delta t = 10$ s. The marginal distributions (bar plots) of λ and k_A^{-1} show that both time scales vary by approximately ± 30 s, and there is no evident modal time scale (peak) in the distributions, indicating the existence of a spectrum of time scales. Interestingly, the joint distribution exhibits a linear correlation between λ and k_A^{-1} , which suggests we can have a relatively accurate estimate of the intrinsic time scale ratio λk_A , despite not having accurate measures of λ and k_A^{-1} separately. Figure 7(b) shows the joint probability distribution of λ and k_A^{-1} for $\phi = 0.12$ and $\Delta t = 10$ s. The marginal distribution of k_A^{-1} shows two modal time scales, peaked at 54 s and 62 s, respectively. Such bimodal distribution of k_A^{-1} can sometime lead to under- or over-estimation of relaxation time scale, which is likely responsible for the unexpected increase in λk_A from $\phi_k = 0.12$ to $\phi_k = 0.19$ for $\Delta t = 20$ s. The marginal distribution of λ shows a single modal time scale at approximately 38.5 s, with narrow

tails of a standard deviation of ~ 1 s. The joint distribution of λ and k_A^{-1} still demonstrates a weak linear correlation, but not as evident as in Fig. 7(a). Both figures show that kaolinite clay suspensions possess multiple microstructural and stress relaxation times. Conventionally, the material’s intrinsic time scales are obtained by plotting the hysteresis area (A_σ) as a function of the sweep time (Δt) and identifying the peak in the A_σ – Δt plot [60, 63, 70]. This procedure requires performing experiments with a range of sweep times; and the effects of thixotropy and viscoelasticity on the identified time scales can be challenging to separate [71]. Here, the reported Bayesian method provides estimates of the material’s intrinsic time scales by directly fitting to the flow curves, without the need for performing experiments of different sweep times.

D. Gravitational aging and microstructural relaxation

We now discuss the origin of “aging”, i.e., the recovery of microstructure in kaolinite clay suspensions. In many colloidal suspensions, the recovery of microstructure is considered to be induced by Brownian motion [21, 23, 36, 50, 92, 93]. We shall see that this may not be the case for kaolinite clay suspensions, since kaolinite particles are essentially non-Brownian. The extent of non-thermal nature of the constituent particles is estimated using the gravitational Péclet number, which is the ratio between the time scale of Brownian motion and the sedimentation time scale [94, 95]:

$$Pe_g = \frac{4\pi r^4 \Delta\rho g}{3k_B T}, \quad (10)$$

where r is the average particle radius, $\Delta\rho$ is the density difference between kaolinite particles and water, g is the gravitational acceleration, k_B is the Boltzmann constant, and T is the Kelvin temperature. Kaolinite particles have a modal nominal diameter of $d \approx 10 \mu\text{m}$ [17, 81], or a particle radius of $r \approx 5 \mu\text{m}$. This leads to a gravitational Péclet number of $Pe_g \sim \mathcal{O}(10^4)$, which indicates that kaolinite particles are non-Brownian in nature and aging in kaolinite suspensions is mainly driven by gravitational settling, rather than Brownian motion. The aging process in kaolinite suspensions can be understood as follows. As kaolinite particles sediment, they pile up onto each other, and aggregate due to electrostatic forces, which constantly generates new microstructures in the suspensions. We should notice that the system does not restore its original state by forming new microstructure. Therefore, we prefer the terminology “restructuring”, instead of “recovery” of microstructure.

This hypothesis allows us to non-dimensionalize our σ – $\dot{\gamma}$ flow curves. To re-scale our shear

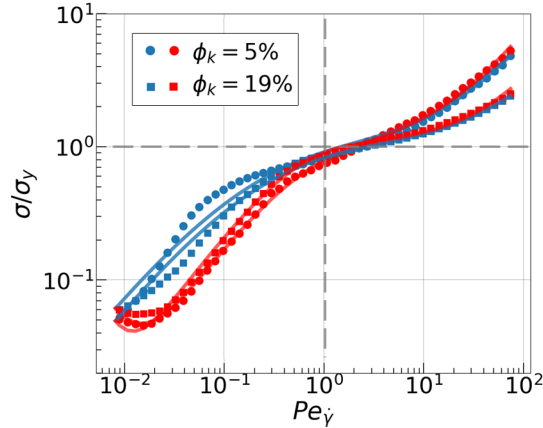


FIG. 8. Normalized stress σ/σ_y vs. the shear Péclet number $Pe_\gamma = 9\eta_w\dot{\gamma}/(2\Delta\rho gr)$. We find that the yield stress σ_y is attained approximately at $Pe_\gamma \sim 1$.

rate, we estimate the shear Péclet number Pe_γ , which is the ratio of the sedimentation time scale and the time scale of the fluid shear (or experimental time scale):

$$Pe_\gamma = \frac{9\eta_w\dot{\gamma}}{2\Delta\rho gr}. \quad (11)$$

Figure 8 shows the normalized stress, scaled using inherent yield stress scale, σ/σ_y as a function of the shear Péclet number Pe_γ . We find that in the re-scaled flow curves, the yield stress σ_y matches approximately at $Pe_\gamma = 1$. Below yield stress, $Pe_\gamma < 1$, the fluid shear is too weak to overrun the gravitational aging. Above yield stress, $Pe_\gamma > 1$, the shear flow is strong enough to rejuvenate the sample from aging, and the suspension starts to fluidize. The yield stress of kaolinite suspensions is a result of the competition between two time scales: the time scale of fluid shear associated with the breakdown of microstructure, and the time scale of gravitational settling associated with the buildup of microstructure. We note that the simple scaling of Pe_γ considers neither the electrostatic force nor the interaction between kaolinite clay particles. Nonetheless, this limitation does not prevent the scaling from qualitatively capturing the yield transition of kaolinite clay suspensions.

IV. CONCLUSIONS

To summarize, we experimentally examine the rheology of kaolinite clay suspensions using a shear rate sweep protocol consisted of consecutive downsweep and upsweep; the flow curves show both yield stress and rheological hysteresis behaviors for various kaolinite volume fractions.

These behaviors are captured by a microstructural viscoelastic model using Markov chain Monte Carlo (MCMC) fitting method. The method also allow us to estimate the rheological properties of the clay suspensions, such as viscosities, stress and microstructural relaxation time scales, and the yield stress. The comparison of stress relaxation time λ and microstructural relaxation time k_A^{-1} suggests that kaolinite clay suspensions are strongly viscoelastic and weakly thixotropic at relatively low volume fractions ($\phi_k < 0.26$), while being almost inelastic and purely thixotropic at the highest volume fractions ($\phi_k = 0.26$). We have also shown that kaolinite suspensions possess multiple or a spectrum of stress and microstructural relaxation time scales. Overall, these results can provide insights for developing predictive models of natural materials like mud and clay, as well as other yield stress materials and known structured fluids.

ACKNOWLEDGMENTS

We thank Yogesh Joshi, Philippe Coussot, Paris Perdikaris, Georgios Kissas, Yibo Yang, and Larry Galloway for helpful discussions. This work was supported by the National Science Foundation (NSF) Grant DMR-1709763 (R.R., P.E.A.), and by the Army Research Office (ARO) Grant W911-NF-16-1-0290 (S.K.A., D.J.J. and P.E.A.), and by ARO Grant W911-NF-20-1-0113 (S.P., D.J.J.).

-
- [1] O. Hungr, S. Leroueil, and L. Picarelli, The varnes classification of landslide types, an update, [Landslides](#) **11**, 167 (2014).
 - [2] D. Pimentel, Soil erosion: A food and environmental threat, [Environ. Dev. Sustain.](#) **8**, 119 (2006).
 - [3] K. B. Dunne and D. J. Jerolmack, What sets river width?, [Sci. Adv.](#) **6** (2020).
 - [4] C. B. Phillips, C. C. Masteller, L. J. Slater, K. B. Dunne, S. Francalanci, S. Lanzoni, D. J. Merritts, E. Lajeunesse, and D. J. Jerolmack, Threshold constraints on the size, shape and stability of alluvial rivers, [Nat. Rev. Earth Environ.](#) **3**, 406 (2022).
 - [5] G. E. Barnes, [Soil Mechanics: Principles and Practice](#) (Palgrave Macmillan, 2010).
 - [6] K. Van Dyke, [Drilling Fluids, Mud Pumps, and Conditioning Equipment](#) (University of Texas at Austin, Petroleum Extension Service, 1998).
 - [7] D. J. Jerolmack and K. E. Daniels, Viewing earth’s surface as a soft-matter landscape, [Nat. Rev. Phys.](#) **1**, 716 (2019).

- [8] P. Coussot, Q. D. Nguyen, H. T. Huynh, and D. Bonn, Viscosity bifurcation in thixotropic, yielding fluids, *J. Rheol.* **46**, 573 (2002).
- [9] F. Da Cruz, F. Chevoir, D. Bonn, and P. Coussot, Viscosity bifurcation in granular materials, foams, and emulsions, *Phys. Rev. E* **66**, 051305 (2002).
- [10] D. Bonn, M. M. Denn, L. Berthier, T. Divoux, and S. Manneville, Yield stress materials in soft condensed matter, *Rev. Mod. Phys.* **89**, 035005 (2017).
- [11] I. Frigaard, Simple yield stress fluids, *Curr. Opin. Colloid Interface Sci.* **43**, 80 (2019).
- [12] P. Coussot, Structural similarity and transition from newtonian to non-newtonian behavior for clay-water suspensions, *Phys. Rev. Lett.* **74**, 3971 (1995).
- [13] S. M. Jogun and C. F. Zukoski, Rheology and microstructure of dense suspensions of plate-shaped colloidal particles, *J. Rheol.* **43**, 847 (1999).
- [14] A. B. D. Brown, S. M. Clarke, P. Convert, and A. R. Rennie, Orientational order in concentrated dispersions of plate-like kaolinite particles under shear, *J. Rheol.* **44**, 221 (2000).
- [15] M. S. Zbik, R. S. Smart, and G. E. Morris, Kaolinite flocculation structure, *J. Colloid Interface Sci.* **328**, 73 (2008).
- [16] V. Gupta, M. A. Hampton, J. R. Stokes, A. V. Nguyen, and J. D. Miller, Particle interactions in kaolinite suspensions and corresponding aggregate structures, *J. Colloid Interface Sci.* **359**, 95 (2011).
- [17] Y. Lin, N. Phan-Thien, J. B. P. Lee, and B. C. Khoo, Concentration dependence of yield stress and dynamic moduli of kaolinite suspensions, *Langmuir* **31**, 4791 (2015).
- [18] R. Neelakantan, F. Vaezi G., and R. S. Sanders, Effect of shear on the yield stress and aggregate structure of flocculant-dosed, concentrated kaolinite suspensions, *Miner. Eng.* **123**, 95 (2018).
- [19] J. Mewis, Thixotropy – a general review, *J. Nonnewton. Fluid Mech.* **6**, 1 (1979).
- [20] H. A. Barnes, Thixotropy – a review, *J. Nonnewton. Fluid Mech.* **70**, 1 (1997).
- [21] J. Mewis and N. J. Wagner, Thixotropy, *Adv. Colloid Interface Sci.* **147-148**, 214 (2009).
- [22] R. G. Larson, Constitutive equations for thixotropic fluids, *J. Rheol.* **59**, 595 (2015).
- [23] R. G. Larson and Y. Wei, A review of thixotropy and its rheological modeling, *J. Rheol.* **63**, 477 (2019).
- [24] F. Moore, The rheology of ceramic slips and bodies, *Trans. Br. Ceram. Soc.* **58**, 470 (1959).
- [25] J. J. Stickel, R. J. Phillips, and R. L. Powell, A constitutive model for microstructure and total stress in particulate suspensions, *J. Rheol.* **50**, 379 (2006).

- [26] A. M. Grillet, R. R. Rao, D. B. Adolf, S. Kawaguchi, and L. A. Mondy, Practical application of thixotropic suspension models, *J. Rheol.* **53**, 169 (2009).
- [27] K. Dullaert and J. Mewis, A structural kinetics model for thixotropy, *J. Nonnewton. Fluid Mech.* **139**, 21 (2006).
- [28] P. R. de Souza Mendes, Modeling the thixotropic behavior of structured fluids, *J. Nonnewton. Fluid Mech.* **164**, 66 (2009).
- [29] P. R. de Souza Mendes, Thixotropic elasto-viscoplastic model for structured fluids, *Soft Matter* **7**, 2471 (2011).
- [30] P. R. de Souza Mendes and R. L. Thompson, A critical overview of elasto-viscoplastic thixotropic modeling, *J. Nonnewton. Fluid Mech.* **187-188**, 8 (2012).
- [31] P. R. de Souza Mendes and R. L. Thompson, A unified approach to model elasto-viscoplastic thixotropic yield-stress materials and apparent yield-stress fluids, *Rheol. Acta* **52**, 673 (2013).
- [32] B. C. Blackwell and R. H. Ewoldt, A simple thixotropic–viscoelastic constitutive model produces unique signatures in large-amplitude oscillatory shear (LAOS), *J. Nonnewton. Fluid Mech.* **208-209**, 27 (2014).
- [33] B. C. Blackwell and R. H. Ewoldt, Non-integer asymptotic scaling of a thixotropic-viscoelastic model in large-amplitude oscillatory shear, *J. Nonnewton. Fluid Mech.* **227**, 80 (2016).
- [34] M. J. Armstrong, A. N. Beris, S. A. Rogers, and N. J. Wagner, Dynamic shear rheology of a thixotropic suspension: Comparison of an improved structure-based model with large amplitude oscillatory shear experiments, *J. Rheol.* **60**, 433 (2016).
- [35] Y. Wei, M. J. Solomon, and R. G. Larson, Quantitative nonlinear thixotropic model with stretched exponential response in transient shear flows, *J. Rheol.* **60**, 1301 (2016).
- [36] Y. Wei, M. J. Solomon, and R. G. Larson, A multimode structural kinetics constitutive equation for the transient rheology of thixotropic elasto-viscoplastic fluids, *J. Rheol.* **62**, 321 (2018).
- [37] M. Agarwal, S. Sharma, V. Shankar, and Y. M. Joshi, Distinguishing thixotropy from viscoelasticity, *J. Rheol.* **65**, 663 (2021).
- [38] Y. M. Joshi, Thixotropy, nonmonotonic stress relaxation, and the second law of thermodynamics, *J. Rheol.* **66**, 111 (2022).
- [39] P. Sollich, F. Lequeux, P. Hébraud, and M. E. Cates, Rheology of soft glassy materials, *Phys. Rev. Lett.* **78**, 2020 (1997).

- [40] P. Sollich, Rheological constitutive equation for a model of soft glassy materials, [Phys. Rev. E](#) **58**, 738 (1998).
- [41] L. Bocquet, A. Colin, and A. Ajdari, Kinetic theory of plastic flow in soft glassy materials, [Phys. Rev. Lett.](#) **103**, 036001 (2009).
- [42] V. Mansard, A. Colin, P. Chauduri, and L. Bocquet, A kinetic elasto-plastic model exhibiting viscosity bifurcation in soft glassy materials, [Soft Matter](#) **7**, 5524 (2011).
- [43] R. S. Jeyaseelan and A. J. Giacomin, Network theory for polymer solutions in large amplitude oscillatory shear, [J. Nonnewton. Fluid Mech.](#) **148**, 24 (2008).
- [44] R. L. Moorcroft, M. E. Cates, and S. M. Fielding, Age-dependent transient shear banding in soft glasses, [Phys. Rev. Lett.](#) **106**, 055502 (2011).
- [45] R. Radhakrishnan, T. Divoux, S. Manneville, and S. M. Fielding, Understanding rheological hysteresis in soft glassy materials, [Soft Matter](#) **13**, 1834 (2017).
- [46] R. L. Moorcroft and S. M. Fielding, Criteria for shear banding in time-dependent flows of complex fluids, [Phys. Rev. Lett.](#) **110**, 086001 (2013).
- [47] M. Moan, T. Aubry, and F. Bossard, Nonlinear behavior of very concentrated suspensions of plate-like kaolin particles in shear flow, [J. Rheol.](#) **47**, 1493 (2003).
- [48] F. Bossard, M. Moan, and T. Aubry, Linear and nonlinear viscoelastic behavior of very concentrated plate-like kaolin suspensions, [J. Rheol.](#) **51**, 1253 (2007).
- [49] Y. M. Joshi, G. K. Reddy, A. L. Kulkarni, N. Kumar, and R. P. Chhabra, Rheological behaviour of aqueous suspensions of laponite: new insights into the ageing phenomena, [Proc. R. Soc. London A](#) **464**, 469 (2008).
- [50] Y. M. Joshi and G. Petekidis, Yield stress fluids and ageing, [Rheol. Acta](#) **57**, 521 (2018).
- [51] C. J. Rueb and C. F. Zukoski, Viscoelastic properties of colloidal gels, [J. Rheol.](#) **41**, 197 (1997).
- [52] A. Abbasi Moud, J. Poisson, Z. M. Hudson, and S. G. Hatzikiriakos, Yield stress and wall slip of kaolinite networks, [Phys. Fluids](#) **33**, 053105 (2021).
- [53] R. Larson, *The rheology and structure of complex fluids* (Oxford University Press, New York, 1999).
- [54] P. E. D. Augusto, V. Falguera, M. Cristianini, and A. Ibarz, Rheological behavior of tomato juice: Steady-state shear and time-dependent modeling, [Food Bioproc. Technol.](#) **5**, 1715 (2012).
- [55] V. Glicerina, F. Balestra, M. Dalla Rosa, and S. Romani, Effect of manufacturing process on the microstructural and rheological properties of milk chocolate, [J. Food Eng.](#) **145**, 45 (2015).

- [56] V. Glicerina, F. Balestra, M. Dalla Rosa, and S. Romani, Microstructural and rheological characteristics of dark, milk and white chocolate: A comparative study, *J. Food Eng.* **169**, 165 (2016).
- [57] M. Krystyjan, M. Sikora, G. Adamczyk, A. Dobosz, P. Tomasiak, W. Berski, M. Łukasiewicz, and P. Izak, Thixotropic properties of waxy potato starch depending on the degree of the granules pasting, *Carbohydr. Polym.* **141**, 126 (2016).
- [58] C. J. Dimitriou and G. H. McKinley, A comprehensive constitutive law for waxy crude oil: a thixotropic yield stress fluid, *Soft Matter* **10**, 6619 (2014).
- [59] M. Geri, R. Venkatesan, K. Sambath, and G. H. McKinley, Thermokinematic memory and the thixotropic elasto-viscoplasticity of waxy crude oils, *J. Rheol.* **61**, 427 (2017).
- [60] T. Divoux, V. Grenard, and S. Manneville, Rheological hysteresis in soft glassy materials, *Phys. Rev. Lett.* **110**, 018304 (2013).
- [61] A. Puisto, M. Mohtaschemi, M. J. Alava, and X. Illa, Dynamic hysteresis in the rheology of complex fluids, *Phys. Rev. E* **91**, 042314 (2015).
- [62] S. M. Fielding, Elastoviscoplastic rheology and aging in a simplified soft glassy constitutive model, *J. Rheol.* **64**, 723 (2020).
- [63] S. Jamali, R. C. Armstrong, and G. H. McKinley, Multiscale nature of thixotropy and rheological hysteresis in attractive colloidal suspensions under shear, *Phys. Rev. Lett.* **123**, 248003 (2019).
- [64] A. Mujumdar, A. N. Beris, and A. B. Metzner, Transient phenomena in thixotropic systems, *J. Nonnewton. Fluid Mech.* **102**, 157 (2002).
- [65] T. Divoux, C. Barentin, and S. Manneville, From stress-induced fluidization processes to herschel-bulkley behaviour in simple yield stress fluids, *Soft Matter* **7**, 8409 (2011).
- [66] M. Fourmentin, G. Ovarlez, P. Faure, U. Peter, D. Lesueur, D. Daviller, and P. Coussot, Rheology of lime paste—a comparison with cement paste, *Rheol. Acta* **54**, 647 (2015).
- [67] D. Perret, J. Locat, and P. Martignoni, Thixotropic behavior during shear of a fine-grained mud from eastern canada, *Eng. Geol.* **43**, 31 (1996).
- [68] S. W. Jeong, J. Locat, J. K. Torrance, and S. Leroueil, Thixotropic and anti-thixotropic behaviors of fine-grained soils in various flocculated systems, *Eng. Geol.* **196**, 119 (2015).
- [69] J. Labanda and J. Llorens, Influence of sodium polyacrylate on the rheology of aqueous laponite dispersions, *J. Colloid Interface Sci.* **289**, 86 (2005).
- [70] S. Jamali and G. H. McKinley, The mnemosyne number and the rheology of remembrance, *J. Rheol.* **66**, 1027 (2022).

- [71] S. Sharma, V. Shankar, and Y. M. Joshi, Viscoelasticity and rheological hysteresis, [arXiv preprint](#), [arXiv: 2203.00890v3 \(2022\)](#).
- [72] R. H. Ewoldt, A. E. Hosoi, and G. H. McKinley, New measures for characterizing nonlinear viscoelasticity in large amplitude oscillatory shear, *J. Rheol.* **52**, 1427 (2008).
- [73] C. J. Dimitriou, R. H. Ewoldt, and G. H. McKinley, Describing and prescribing the constitutive response of yield stress fluids using large amplitude oscillatory shear stress (LAOStress), *J. Rheol.* **57**, 27 (2013).
- [74] J. C.-W. Lee, K. M. Weigandt, E. G. Kelley, and S. A. Rogers, Structure-property relationships via recovery rheology in viscoelastic materials, *Phys. Rev. Lett.* **122**, 248003 (2019).
- [75] G. J. Donley, P. K. Singh, A. Shetty, and S. A. Rogers, Elucidating the G'' overshoot in soft materials with a yield transition via a time-resolved experimental strain decomposition, *Proc. Natl. Acad. Sci. U.S.A.* **117**, 21945 (2020).
- [76] J. B. Freund and R. H. Ewoldt, Quantitative rheological model selection: Good fits versus credible models using Bayesian inference, *J. Rheol.* **59**, 667 (2015).
- [77] M. Mahmoudabadbozchelou, M. Caggioni, S. Shahsavari, W. H. Hartt, G. Em Karniadakis, and S. Jamali, Data-driven physics-informed constitutive metamodeling of complex fluids: A multifidelity neural network (MFNN) framework, *J. Rheol.* **65**, 179 (2021).
- [78] M. Mahmoudabadbozchelou and S. Jamali, Rheology-informed neural networks (RhINNs) for forward and inverse metamodeling of complex fluids, *Sci. Rep.* **11**, 12015 (2021).
- [79] M. Mahmoudabadbozchelou, G. E. Karniadakis, and S. Jamali, nn-PINNs: Non-newtonian physics-informed neural networks for complex fluid modeling, *Soft Matter* **18**, 172 (2022).
- [80] M. Mahmoudabadbozchelou, K. M. Kamani, S. A. Rogers, and S. Jamali, Digital rheometer twins: Learning the hidden rheology of complex fluids through rheology-informed graph neural networks, *Proc. Natl. Acad. Sci.* **119**, e2202234119 (2022).
- [81] A. Seiphoori, A. Gunn, S. Kosgodagan Acharige, P. E. Arratia, and D. J. Jerolmack, Tuning sedimentation through surface charge and particle shape, *Geophys. Res. Lett.* **48**, e2020GL091251 (2021).
- [82] P. Marjoram, J. Molitor, V. Plagnol, and S. Tavaré, Markov chain Monte Carlo without likelihoods, *Proc. Natl. Acad. Sci. U.S.A.* **100**, 15324 (2003).
- [83] N. Metropolis, A. W. Rosenbluth, M. N. Rosenbluth, A. H. Teller, and E. Teller, Equation of state calculations by fast computing machines, *J. Chem. Phys.* **21**, 1087 (1953).

- [84] W. K. Hastings, Monte Carlo sampling methods using Markov chains and their applications, *Biometrika* **57**, 97 (1970).
- [85] H. Haario, E. Saksman, and J. Tamminen, An adaptive Metropolis algorithm, *Bernoulli* **7**, 223 (2001).
- [86] C. Andrieu and J. Thoms, A tutorial on adaptive MCMC, *Stat. Comput.* **18**, 343 (2008).
- [87] T. A. Oliver, G. Terejanu, C. S. Simmons, and R. D. Moser, Validating predictions of unobserved quantities, *Comput. Methods Appl. Mech. Eng.* **283**, 1310 (2015).
- [88] W. H. Herschel and R. Bulkley, Konsistenzmessungen von Gummi-Benzollösungen, *Kolloid-Z.* **39**, 291 (1926).
- [89] Y. M. Joshi, A model for aging under deformation field, residual stresses and strains in soft glassy materials, *Soft Matter* **11**, 3198 (2015).
- [90] B. Rand and I. E. Melton, Particle interactions in aqueous kaolinite suspensions: I. effect of pH and electrolyte upon the mode of particle interaction in homoionic sodium kaolinite suspensions, *J. Colloid Interface Sci.* **60**, 308 (1977).
- [91] S. Chattopadhyay, S. Nagaraja, and S. Majumdar, Effect of adhesive interaction on strain stiffening and dissipation in granular gels undergoing yielding, *Commun. Phys.* **5**, 126 (2022).
- [92] K. Dullaert and J. Mewis, Thixotropy: Build-up and breakdown curves during flow, *J. Rheol.* **49**, 1213 (2005).
- [93] Y. Wei, M. J. Solomon, and R. G. Larson, Time-dependent shear rate inhomogeneities and shear bands in a thixotropic yield-stress fluid under transient shear, *Soft Matter* **15**, 7956 (2019).
- [94] G. L. Hunter and E. R. Weeks, The physics of the colloidal glass transition, *Rep. Prog. Phys.* **75**, 066501 (2012).
- [95] S. Pradeep and L. C. Hsiao, Contact criterion for suspensions of smooth and rough colloids, *Soft Matter* **16**, 4980 (2020).